ORIGINAL PAPER

The Effects of Cooling on Fine-Grained Sandstone in Relation to Wellbore Injection of Carbon Dioxide

Nikolaos Reppas[1,2] · Colin T. Davie[1] · Yilin Gui[3,4,5] · Ben Wetenhall[1] · Samuel P. Graham[1,6]

Abstract

In Carbon Capture and Storage (CCS) procedures, it is important to determine the stability of the wellbore during carbon dioxide (CO_2) injection and part of this involves assessing stresses on the rock near the wellbore due to changes in temperature and pressure. To address this, this study investigated the influence of cooling on the mechanical properties of a sandstone typical of those found in the central and southern North Sea. A series of uniaxial and triaxial compression tests was conducted on dry and saturated sandstone samples to determine the effects of cooling on the strength and stiffness under different confining pressures. The elastic modulus, shear modulus, bulk modulus and Poisson's ratio were determined for three temperature conditions and three pressures representing different depths in a wellbore. Two methods, the International Society of Rock Mechanics (ISRM) and Wood's (Soil behaviour and critical state soil mechanics. Cambridge University Press, Cambridge, 1990), were used to determine the mechanical properties of the rock during the Uniaxial Compressive Strength (UCS) tests. For the triaxial test, only Wood's (1990) method was applied due to the existence of confining pressure. Microstructural analysis on thin sections of the sandstones under plane and crossed polarised light conditions in the deformed and undeformed state was conducted to elucidate deformation mechanisms and aid interpretation of experimental results. It was identified that both an increase in confinement and a reduction in temperature, increased the strength of the sandstone and reduced the Poisson's ratio. Additionally, by decreasing the temperature, especially in the UCS test the material dilated less. This is an important outcome as expanding the results to a wellbore stability problem, brittle behaviour may be more apparent and damage may occur when sub-zero injection temperatures are applied, especially at the wellbore head, where confinement is low.

Highlights

- UCS and triaxial tests on Stainton Sandstone at 15 ℃, − 5 ℃ and − 10 ℃ were used to determine the influence of temperature drop on Poisson's ratio and different mechanical moduli.
- Wood's (1990) method for determining the mechanical properties of rock using critical state mechanics can also be applicable to UCS tests.
- Microscopic analysis of sandstone sample before and after the UCS and triaxial tests indicated dilation and grain realignment, which result in Poisson's ratios greater than 0.5.
- Expanding the experimental results to CCS challenges, the wellbore head is the most vulnerable to sub-zero temperatures due to lack of confinement.

✉ Nikolaos Reppas
   N.Reppas2@newcastle.ac.uk

1   School of Engineering, Newcastle University, Newcastle upon Tyne NE1 7RU, UK

2   Net-Zero Geosystems Limited, London SE26 6UT, UK

3   School of Civil and Environmental Engineering, Queensland University of Technology, Brisbane 4000, Australia

4   Centre for Materials Science, Queensland University of Technology, Brisbane 4000, Australia

5   Group of Sustainable Engineered Construction Materials, Queensland University of Technology, Brisbane 4000, Australia

6   School of Geosciences, University of Edinburgh, Edinburgh ED9 4FE, UK

List of Symbols

v	Poisson's ratio
σ_1	Axial stress
σ_3	Radial stress
$\sigma_{\max D}$	The maximum uniaxial compressive strength of a sample with certain diameter D
$\sigma_{\max (D=50)}$	The maximum reference uniaxial compressive strength of a 50-mm-diameter sample
ε_a	Axial strain
ε_c	Circumferential strain
ε_p	Volumetric strain
ε_q	Triaxial Shear strain
E	Young's modulus (MPa)
$E_{\tan}$	Tangent Young's modulus (MPa)
$E_{\sec}$	Secant Young's modulus (MPa)
G	Shear modulus (MPa)
K	Bulk modulus (MPa)
M_{cs}	Slope of critical state line
M	The parameter controls the shape of the bounding surface
p'	Current effective stress on the yield surface (MPa)
p_{co}'	Maximum pre-consolidated pressure (MPa)
q	Deviatoric stress (MPa)
R	Material parameter in bounding surface

1 Introduction

Carbon Capture and Storage (CCS), is a promising approach to reduce greenhouse gases and help prevent global warming by safely storing liquid carbon dioxide (CO_2) in geological rock formations (Haszeldine 2009). CO_2 may be stored permanently in depleted oil and gas fields, deep saline aquifers, or coal seams (Jin et al. 2012). However, to date only a limited number of projects have been undertaken at scale (Martin-Roberts et al. 2021), for example Sleipner in the North Sea, In-Sallah in Algeria, and Snøhvit in the Barents Sea (Chadwick et al. 2004; Armitage et al. 2011; Eiken et al. 2011; Hansen et al. 2013). The UK's first decarbonised industrial cluster will be the Net Zero Teesside in the Southern North Sea, where CO_2 will be stored in Triassic Bunter Sandstone of the Endurance field (Gluyas and Bagudu 2020; Page et al. 2020; Sutherland et al. 2020; Nevicato 2022).

The mechanical properties of the overburden sequence control not only the amount of CO_2 that can be stored, but also the maximum allowable well-bottom pressure and, therefore, the rate of injection. To ensure successful injection and the stability of long-term storage, reliable geomechanical characterisation of the wellbore, reservoir, and sealing formation rock is required in order to understand the capabilities of potential storage sites and to minimise leakage risk, and failure of the injection infrastructure (Mathias

et al. 2009; Rutqvist 2012). A particular challenge in CO_2 injection wells is the effect of thermal loading due to the temperature difference between the injected CO_2 and the surrounding rock (Mukherjee and Brill 1999; Paterson et al. 2010). If CO_2 is colder than the wellbore rock formation, this can cause thermal contraction and induce stresses, which can induce rock fracturing and damage. The CO_2 delivery method, usually either by pipeline or pumping from ships, will determine the temperature and pressure of the CO_2 in the wellbore and reservoir. In pipeline CO_2 transportation, temperature difference can be extremely high due to the injection of high pressurised CO_2 into a low pressurised wellbore, causing CO_2 expansion and temperature drop due to the Joule–Thomson effect. (Oldenburg 2007; Ziabakhsh-Ganji and Kooi 2014; Wang et al. 2019b). For CO_2 transportation offshore and injection by ships, the CO_2 is stored in the ship at specific temperature and pressure conditions close to the triple point (around – 52 °C and 0.6–0.7 MPa), in order to keep containment of the CO_2 mixture in near-liquid form (Barrio et al. 2005). This study assumes ship transportation and storage in the central and southern North Sea, which has a capacity of more than 40 Gt for CO_2 storage.

Injection pressures in excess of 5 MPa are usually employed in order for the CO_2 to remain in the liquid or supercritical phase (Vilarrasa et al. 2013). Geological formation temperatures at the seabed are typically around 4 °C (Aursand et al. (2017)). Normally, the CO_2 is heated up to the temperature of the wellbore head formation to avoid large thermal fluctuations. However, this can be financially and energetically burdensome, therefore injecting at lower temperatures could be advantageous. For this reason, studies have been undertaken on injecting CO_2 at temperatures lower than that of the wellbore head, in liquid state (Rayward-Smith and Woods 2011; Silva et al. 2011; Li et al. 2015). However, cold CO_2 injection can result in a large thermal contrast between the wellbore wall and the surrounding rock leading to a reduction in effective stresses in the rock, which brings the stress state closer to failure (Segall and Fitzgerald 1998).

Throughout the literature, extensive laboratory research experimentally characterises the mechanical properties of sandstone and other rocks at high temperatures (range from 25 to 800 ℃) in the context of geothermal energy applications and true subsurface conditions (ranging from 30 to 1200 ℃) (Rao et al. 2007; Wu et al. 2013; Kong et al. 2016; Zhu et al. 2016; Yang et al. 2017, 2021). UCS, Brazilian, three point bending and triaxial tests are routinely conducted to describe the behaviour of rock under high temperature and pressure effects (Yang et al. 2017). Results showed that rock properties vary as function of temperature (Sun et al. 2020). Whilst high-temperature characterisations are beneficial for geothermal energy applications and conventional

CO_2 injection, investigation of mechanical properties of sandstones at low temperatures ($T < 0$ °C) are mainly focussing on freeze–thaw loading such as the work of Liping et al. (2019), Yahaghi et al. (2021), Huang et al. (2022), Fakhri et al. (2023) and Yu et al. (2023). UCS and triaxial tests for mechanical characterisation of sandstone at certain sub-zero temperatures are limited according to Kodama et al. (2019). Some of the studies are the low-temperature UCS tests by Liu et al. (2020) and Zhang et al. (2023), demonstrated a reduction in sandstone's strength with decreasing temperature. Some examples of triaxial tests at low-temperature conditions for sandstone are presented in the work of Bai et al. (2020), Wu et al. (2020), Huang et al. (2022) and Shu et al. (2023) who suggested that the peak strength and the elastic modulus of rock increased with a decrease in the temperature for constant confining pressure. Although the mechanical properties of different sandstones under low-temperature conditions have been analysed, data pertinent to sandstones useful to CCS projects in the North Sea basin are sparse. This paper aims to address this knowledge gap through a laboratory testing programme on fine-grained UK sandstone, considering not just the low-temperature, low-stress scenario, but also a range of confining stresses relevant to reservoir depths for existing CCS schemes within the North Sea basin. We use a Carboniferous sandstone from coal measures sequences as an analogue for our reservoir sandstone. Coal measures sandstones are abundant at depth within the North Sea basin, particularly in the southern part (Leeder and Hardman 1990).

2 Experimental Setup and Methodology

2.1 The Testing Material and the Experimental Procedure

The aim of this study was to explore how the mechanical properties of sandstone evolve at low-temperatures under a range of confining stresses relevant to the near-wellbore region during subsurface storage and injection of CO_2. Samples of carboniferous coal-measures sandstone from onshore UK (Stainton Quarry, UK) were used as a representative analogue of common reservoir rocks throughout the North Sea basin to understand how low temperatures may influence the mechanical behaviour of the near wellbore region in practical scenarios (Hawkins 1978; Heinemann et al. 2012; Hangx et al. 2013; Agada et al. 2017).

The rock can be described according to the British Standards, as a strong medium bedded, buff coloured with fine brown speckle, medium grained, clastic sandstone. The rock was extracted from a 10.5 m face below 3.6 m of overburden. The location of the quarry from where the rock was collected is 2 miles east of Barnard Castle, UK. The porosity of the rock according to the technical data sheet of the quarry is approximately 17%. The dry density of the rock was calculated to be 2.3 g/cm³.

In total, twenty-seven samples were tested, as listed in Table 1. The samples were cylindrical with the height to diameter ratio 2:1, as recommended by ISRM (Ulusay 2014). The samples were cored from two blocks, extracted from the same depth and their dimensions and weight can be seen in Table 1. Strain gauges were attached and "Araldite rapid epoxy" was used to waterproof them. Each sample was then saturated in a water bath under vacuum for approximately 24 h in a NaCl solution with a molar concentration of 0.6 mol·L^{-1} to represent North Sea conditions.

In the present work, the experiments are conducted under pressure conditions representative of storage in current and potential reservoirs in the North Sea basin (Gluyas and Bagudu 2020). Here the average water depth at seabed is 80 m according to Sündermann and Pohlmann (2011), corresponding to a hydrostatic pressure of 0.8 MPa, which is small enough to assume that the mechanical properties of the rock at the seabed are represented by UCS tests in this research (and comparable to operations in the Sleipner field (Eiken et al. 2011)). Additionally, a fully saturated formation is subjected to vertical gradients of in situ stresses range from 23 to 25 kPa/m (Kazemi 1969; Zoback and Zoback 2002; Ma and Zhao 2018). For this reason, in this research, the assumed vertical gradient of in situ stresses is 24 kPa/m, which is the average of this range. Triaxial tests are conducted at 12.5 MPa and 24 MPa confining pressure, which are representative of conditions at around 550 m depth (mid-depth of the wellbore) and 1000 m (reservoir entry point), respectively. For the selection of those depths the active CO_2 project Sleipner field in the North Sea basin was considered, with injection depths range from 800 to 1000 m (Eiken et al. 2011).

The selected temperatures for the experimental tests were based on previous injection studies. Vilarrasa et al. (2013) examined a temperature range of injection based on a pilot injection 'Hontomin' in Spain (Carrera et al. 2011), varying from − 20 ℃ for liquid phase injection to 40 ℃ for supercritical phase injection and injection pressures varied from 4.2 to 8 MPa. Additionally, Silva (2015) studied injection rates between − 10 and 40 ℃, and injection pressures varying from 4 MPa to nearly 10 MPa. Roy et al. (2018) studied range of injection between − 15 and 20 ℃. All these studies set the lower temperature limit of the CO_2 injection to − 20 ℃, since that the freezing point of brine is approximately − 21 ℃ (Roy et al. 2018). Based on the research of Vilarrasa et al (2013), for an injection temperature of − 20 ℃, temperature at 1000 m depth would be around − 10 ℃ due to heat exchange with the surrounding rock, which temperature increases due to geothermal

Table 1 Characteristics of the tested samples

Temperature	Sample	Diameter (mm)	Length (mm)	Dry mass (g)	Wet mass (g)	Moisture content %
UCS tests dry sandstones						
15 ℃	A′	59.3	129.31			
	B′	59.3	129.32			
	C′	59.3	130.22			
UCS tests saturated sandstones						
15 ℃	A	37.62	83.37	199.44	215.20	7.32
	B	37.61	84.65	202.46	217.13	6.76
	C	37.61	82.85	198.21	214.30	7.51
– 5 ℃	D	37.89	81.39	206.95	226.90	8.79
	E	37.83	77.88	197.88	210.33	5.92
	F	37.81	81.16	202.56	217.25	6.76
– 10 ℃	G	37.82	84.18	212.56	225.72	5.83
	H	37.80	80.14	199.08	213.73	6.85
	I	38.12	84.24	210.14	224.87	6.55
Triaxial tests 12.5 MPa saturated sandstones						
15 ℃	1	37.65	82.45	208.11	221.12	5.88
	2	37.60	83.14	199.18	214.22	7.02
	3	37.40	80.76	191.13	208.55	8.35
– 5 ℃	4	37.79	79.31	201.60	214.50	6.01
	5	37.81	83.06	209.27	223.91	6.54
	6	37.91	81.74	203.68	218.80	6.91
– 10 ℃	7	37.92	80.91	204.30	218.31	6.42
	8	37.81	79.29	199.98	212.94	6.09
	9	37.79	79.49	200.57	215.17	6.79
Triaxial tests 24 MPa saturated sandstones						
15 ℃	I	37.42	84.40	200.80	213.22	5.82
	II	37.58	82.86	196.65	213.71	7.98
	III	37.80	83.25	208.4	221.32	5.84
– 5 ℃	IV	37.79	83.30	208.91	221.10	5.51
	V	37.82	84.87	213.10	227.50	6.33
	VI	37.78	83.24	209.21	223.14	6.24
– 10 ℃	VII	37.88	80.35	202.01	216.57	6.72
	VIII	38.01	83.76	212.57	226.45	6.13
	IX	37.94	82.25	207.65	222.02	6.47

gradient with a rate of 33 °C/km. This shows that sub-zero temperatures can be present even at significant depths, highlighting the relevance of low-temperature experiments for simulating CO2 injection conditions. For this reason, we examine the influence of low-temperatures relevant to injection of CO_2 from ships and conduct experiments at 15 ℃ (room temperature), – 5 ℃ and – 10 ℃, which can be representative temperatures inside the wellbore, depended on the selected CO_2 injection condition. Young's modulus (E), Poisson's ratio (v), bulk modulus (K) and shear modulus (G) are used to characterise the rock.

To achieve the target temperatures, the saturated samples were placed in a freezer for 35 min to reach – 5 ℃, and 44 min to reach -10 ℃. The freezer's temperature was – 20 ℃ and the time required to achieve these temperatures was calculated by freezing saturated samples from the same rock block with a hole drilled into the centre into which a thermometer was inserted. For the UCS test, after freezing was achieved, each saturated sandstone sample was placed inside an Instron environmental chamber for 10 min prior to loading with the chamber set to the test temperature. In this way temperature loss due to transportation of the sample from the freezer to the environmental chamber was addressed. For the triaxial tests, the frozen sample was placed in a 38 mm diameter Hoek cell which was then placed inside the environmental chamber for 30 min prior to loading with the temperature

set to test conditions. This ensured that both the Hoek cell and the sample reach the required temperature before any loads were applied. The temperature was maintained constant during testing. For each triaxial test, the confining pressure was increased at a constant rate of 1 MPa/min up to the maximum before axial stress was applied. Both uniaxial and triaxial compression tests were performed under axial strain-control with an axial displacement rate of 0.1 mm/min. A typical sample, the Hoek cell and the environmental chamber can be seen in Fig. 1.

2.2 Methods Used for the Analysis of the Experimental Results

Poisson's ratio in geotechnical engineering is typically considered as a fixed constant that can take values smaller than 0.5, which is representative of a fully elastic behaviour. Smaller values indicate a stiffer material, which can fracture more easily as brittleness increases with reduction in Poisson's ratio (Rickman et al. 2008; Zhang et al. 2016). Poisson's ratio, v, can be expressed as follows:

$$v = \frac{\text{Young's modulus}(E)}{\text{slope of stress} - \text{lateral strain curve}}. \tag{1}$$

In this study, tangent and secant Young's moduli were used for the determination of the tangent and secant Poisson's ratio, respectively, as seen in Fig. 2. For the UCS tests, tangent Poisson's ratio was calculated using the linear part of the stress–strain curve. This was found by selecting the range of the stress–strain curve lying ±20% above and below the value of the centre point of the stress interval (50% of the maximum stress and shown as E_{tan} in Fig. 2). The range of the stress interval can differ but its effect is negligible on the Young's modulus and consequently on Poisson's ratio (Dong et al. (2021)). The secant Poisson's ratio was determined from the slope of the axial-volumetric strain curve
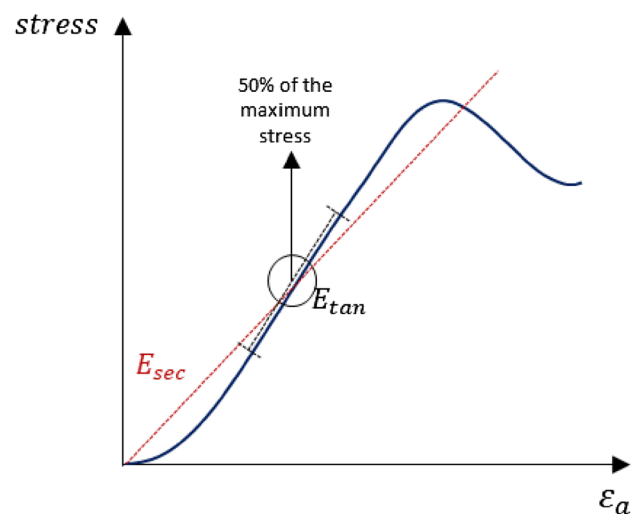

Fig. 2 Tangent and Secant measurements based on Małkowski et al. (2018)

corresponding to the span from the origin to 50% of the uniaxial compressive strength (Shown as E_{sec} in Fig. 2).

The bulk and shear moduli can be calculated using the following formulae:

$$K = \frac{E}{3(1 - 2v)} \tag{2}$$

$$G = \frac{E}{2(1 + v)}. \tag{3}$$

Apart from the ISRM method used for the UCS tests, many geomechanical models for sandstones are built from concepts of critical state soil mechanics (Gerogiannopoulos and Brown 1978; Cuss et al. 2003; Singh et al. 2005; Shen et al. 2018). Wood (1990) expanded critical state soil mechanics theory to describe brittle rock or work-softening materials and the material moduli (E, v, K and G) can be
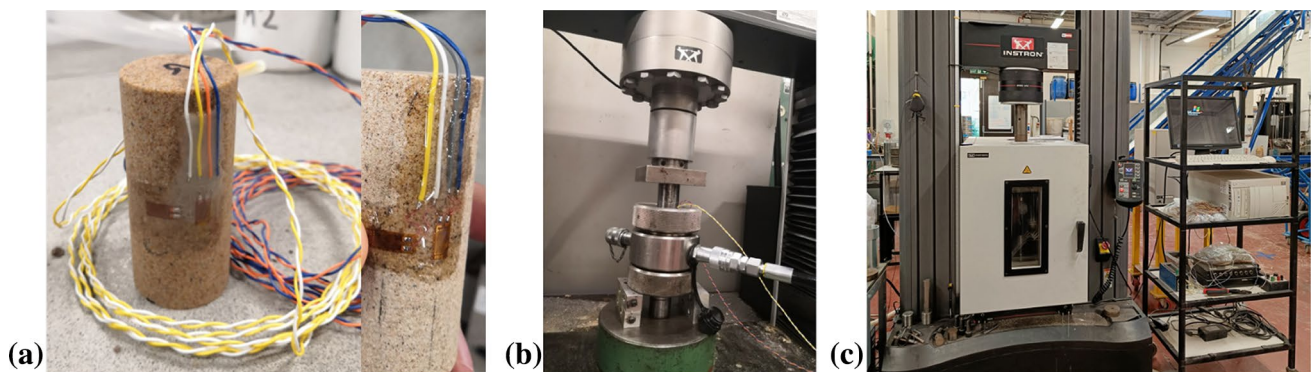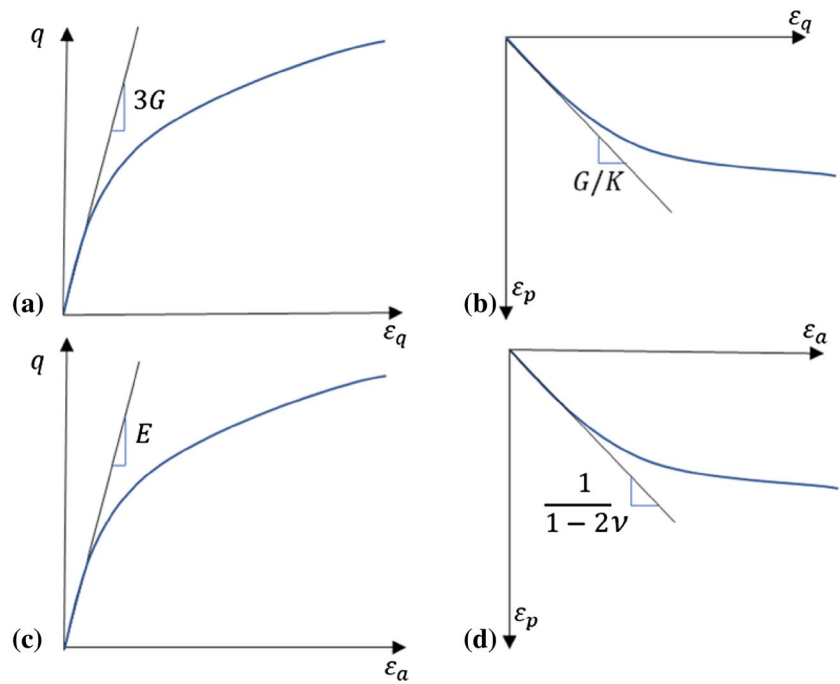

Fig. 1 **a** Example sample with strain gauges attached, **b** Hoek cell equipment, **c** Environmental chamber with Hoek cell inside

Fig. 3 **a** Shear modulus slope, **b** bulk modulus calculation, **c** Young's modulus slope **d** Poisson's ratio calculation (Wood 1990)

calculated from the slope of the different plots presented in Fig. 3. Wood's (1990) method was used as the ISRM method is only appropriate for UCS tests.

According to Wood (1990), Poisson's ratio can be expressed as the ratio between the volumetric strain increment $d\varepsilon_p$ and the triaxial shear strain increment $d\varepsilon_q$. The deviatoric stress q, the volumetric strain increment and the shear strain increment can be presented as follows:

$$q = \sigma_1 - \sigma_3 \tag{4}$$

$$d\varepsilon_p = d\varepsilon_a + 2d\varepsilon_c \tag{5}$$

$$d\varepsilon_q = 2(d\varepsilon_a - d\varepsilon_c)/3, \tag{6}$$

where σ_1 & σ_3 are the axial and radial stresses or confining stress and $d\varepsilon_a$ & $d\varepsilon_c$ are the axial and circumferential strain increments.

3 Experimental Results

3.1 UCS Results

Results from the UCS tests for dry (Fig. 4) and fully saturated samples (Figs. 5, 6 and 7) are presented in this section. From the results in dry conditions the rock can be classified according to BS EN ISO 14689–1 as strong sandstone (BS 2015). As the dry tested samples were of different diameter, size effect was considered to estimate the peak strength. According to
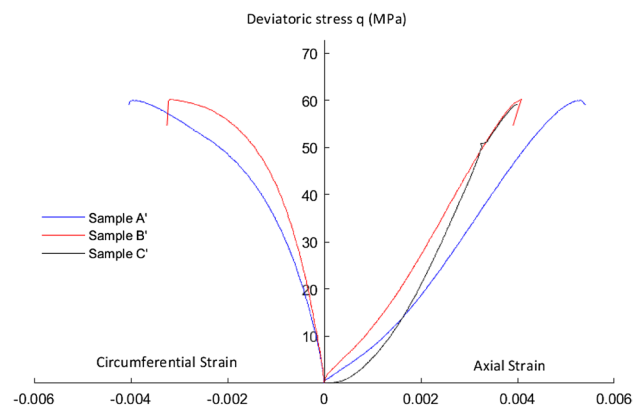

Fig. 4 UCS test—Dry sandstone at 15 ℃

Masoumi et al. (2018) the relation to describe the size effects of the UCS test is as follows:

$$\sigma_{\max D} = \sigma_{\max (D=50)} \left(D/50 \right)^{-k}, \tag{7}$$

where $\sigma_{\max D}$ & $\sigma_{\max (D=50)}$ are the maximum uniaxial compressive strength of a sample with certain diameter D and of a 50-mm-diameter sample, respectively, and k is rock coefficient range from 0.1 to 0.3 for isotropic rock.

For the current research, in order to compare the maximum strength of the dry and saturated samples (Figs. 4 and 5), k was considered equal to 0.18 as suggested for sedimentary rocks and sandstones by Hoek and Brown (1980), Hawkins (1998), Yoshinaka et al. (2008) and Masoumi et al. (2016). The average UCS strength value was determined for the three dry and three saturated tests at − 15℃ condition as presented in Table 2. Using Eq. (7), the $\sigma_{\max (D=50)}$ was
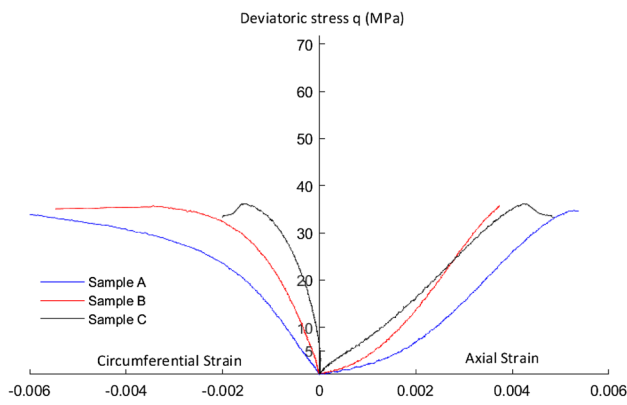
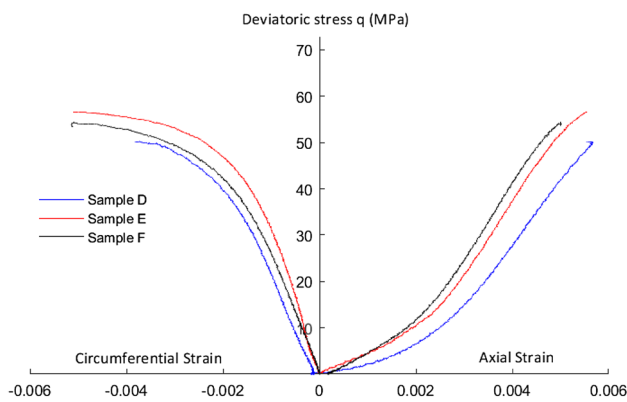**Fig. 5** UCS test—Saturated sandstone at 15 ℃
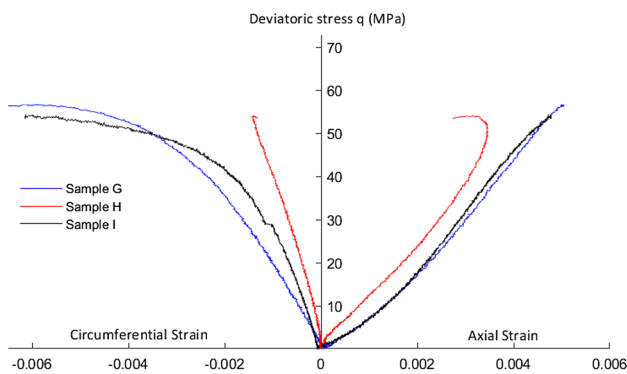

Fig. 6 UCS test—Saturated sandstone at – 5 ℃

Fig. 7 UCS test—Saturated sandstone at – 10 ℃

Table 2 Maximum UCS strength of the dry and saturated tested sandstones at 15 ℃, average maximum value of them and comparison to the average maximum reference value for a theoretical 50 mm diameter-sample

Sample ID	D (mm)	σ_{maxD} (MPa)	Average, σ_{maxD} (MPa)	Average, $\sigma_{max(D=50)}$ (MPa)
Dry sandstone UCS 15 °C				
Sample A′	59.3	60		
Sample B′	59.3	60.2	59.8	61.2
Sample C′	59.3	59.1		
Saturated sandstone UCS 15 ℃				
Sample A	37.62	34.7		
Sample B	37.61	35.6	35.4	35.7
Sample C	37.61	36.1		

significantly to the average maximum UCS strength values of the sample sizes presented in Table 2.

Comparing the dry and saturated UCS tests at 15 ℃, after comparing the $\sigma_{D=50}$, it can be seen that the peak strength is higher in the dry sample by approximately 40%, which is in agreement with the testing results presented by Romana and Vásárhelyi (2007). The saline water decreases the strength of the material in room temperature conditions. For the lower temperatures: – 5 ℃ and – 10 ℃, the strength increases due to ice formation inside the pores and fissures of the sandstone. For the saturated samples, it can be determined that when changing from 15 to – 5 ℃, where ice forms, the strength of the material increases by more than 35%. However, when changing the temperature from – 5 to – 10 ℃ the peak strength remains approximately constant (Figs. 5, 6 and 7). This indicates that ice has already formed at – 5 ℃ and further temperature drop does not influence the strength of the rock significantly. Additionally, lower temperatures decrease the ductility and deformability of the sandstones. The post-failure phase indicates this ductility decrease effect, as seen by comparing figures (Figs. 5, 6 and 7). Specifically, in the 15 °C UCS test, the dilation of the material can be seen at the post-failure phase (see Fig. 5), while at freezing temperatures, the rock mostly fails once it reaches the peak strength (Figs. 6, 7). Masri et al. (2014) outlined this trend but for temperatures greater than sub-zero using a range from 20 to 250 ℃.

In Fig. 8 the tested samples are presented showing the different types of failure. From Fig. 8a, it can be seen that the sandstones tested at room temperature and 15℃ obtained a double shear or shear along a single plane, in line with the findings of Everall and Sanislav (2018). For lower temperatures, some parts of the sandstone were detached, especially for – 10 ℃, as seen in Fig. 8c. This can be explained by ice formation and a decrease in Poisson's ratio causing

estimated for the dry and saturated condition as presented in Table 2. Specifically, for a sample with diameter $D = 50$ mm, the max UCS strength was 61 MPa for dry test and 35.7 for the saturated test at 15 ℃. Those two values did not vary

multi-fracturing during the test. The post peak behaviour of sample H (Fig. 7) can be explained by the ice formation and indicates a collapse of part of the sample, as seen in Fig. 7c.

The ISRM method and Wood's method are compared in terms of the Poisson' ratio in Table 3. That comparison is made to suggest that Wood's method can be used also for UCS tests, as UCS can be simplified as a triaxial test with 0 MPa confining pressure. The Young's modulus is also presented. The ISRM and Wood's methods for both tangent and secant moduli agree with similar results, indicating that the triaxial approach of Wood (1990) can be applied to UCS tests for the estimation of Poisson's ratio. This can permit comparison of the UCS and triaxial test results.

To further examine the temperature effects on the mechanical behaviour of sandstone, the secant bulk and tangent and secant shear moduli from the UCS tests, calculated based on the respective tangent and secant Young's modulus (ISRM method) and on the slopes of the curves presented in Fig. 2 (Wood's (1990) method), are outlined in Fig. 9a, b respectively. Whiskers show the maximum and minimum value of each test with the box representing the average value of the modulus. Full results from Sample C, Sample C' and Sample H are not shown since for Sample C' the strain circumferential gauge failed, possibly due to cable crushing by the axial piston, Sample C had a Poisson's ratio significantly lower than the other two tests, and for Sample H there was a crack at the attachment point to the strain gauge.

Table 3 Tangent and Secant Young's modulus, Tangent and Secant Poisson's ratio, Comparison between two methods ISRM and Wood's

Samples	Max UCS strength, MPa	Young modulus, (E), GPa		v, ISRM	v, Woods method
Room temperature 15 ℃ saturated sandstone UCS					
Sample A	34.7	Tangent	9.5	0.78	0.78
		Secant	5.2	0.35	0.35
Sample B	35.6	Tangent	13.0	0.64	0.62
		Secant	7.5	0.28	0.27
Sample C	36.1	Tangent	10.1	0.54	0.53
		Secant	7.7	0.17	0.14
Freezing – 5 ℃ saturated sandstone UCS					
Sample D	51.2	Tangent	16.6	0.68	0.68
		Secant	6.5	0.27	0.27
Sample E	56.5	Tangent	16.4	0.64	0.62
		Secant	7.3	0.22	0.22
Sample F	54.3	Tangent	16.1	0.76	0.75
		Secant	7.8	0.30	0.30
Freezing – 10 ℃ saturated sandstone UCS					
Sample G	56.6	Tangent	15.2	0.61	0.60
		Secant	10.4	0.32	0.32
Sample H	54.0	Tangent	12.2	0.33	0.33
		Secant	11.4	0.23	0.22
Sample I	54.2	Tangent	14.1	0.61	0.60
		Secant	7.7	0.30	0.29

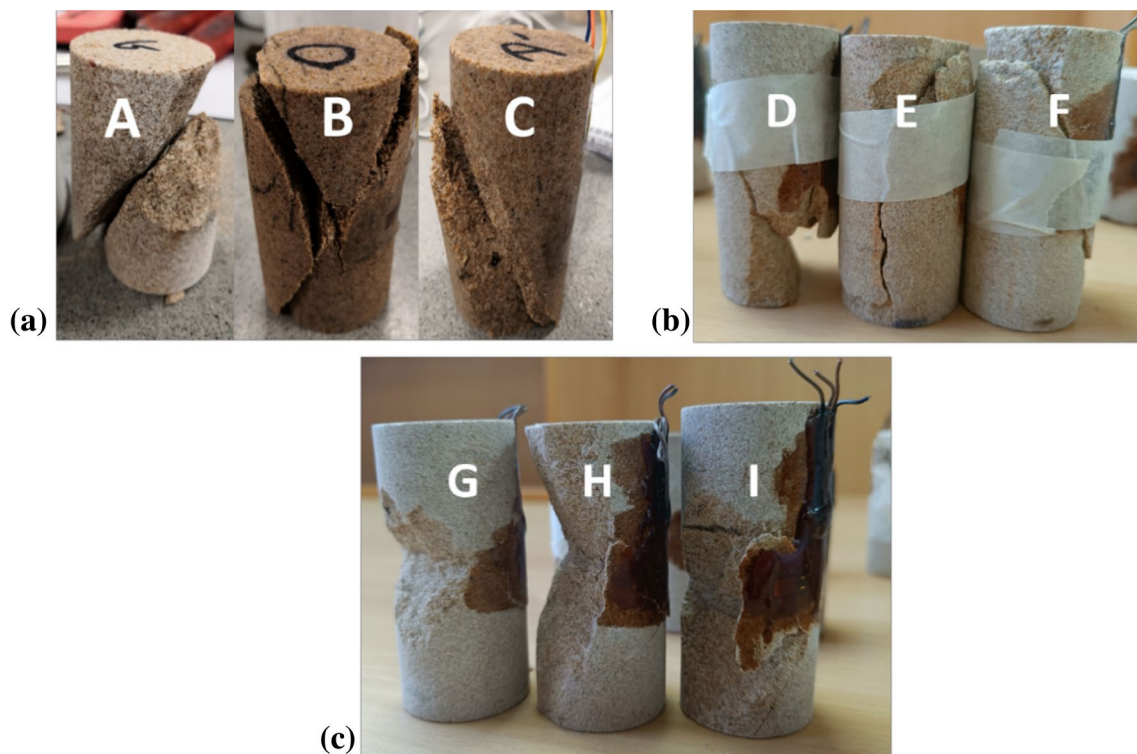**Fig. 8** Saturated samples after testing **a** 15 ℃ **b** – 5 ℃ **c** – 10 ℃

Selecting the linear part of the UCS stress–strain curve with a ±20% range from the middle point to calculate the tangent modulus, the Poisson's ratio is larger than 0.5 for both the dry and saturated samples, suggesting dilation in the sandstone. According to Dong et al. (2021), despite the fact that the theoretical maximum of Poisson's ratio is 0.5, soft rocks see a rapid increase in Poisson's ratio beyond this value during loading. Specifically, the volume increases as grains realign. Due to this dilation of the material, both Wood's and the ISRM methods of calculation imply that the average tangent bulk modulus would have a negative value, and although the values calculated by the two methods are consistent, this is a non-physical result and for this reason is not presented in Fig. 9. Despite the dilation, for the secant calculations, the Poisson's ratio is consistently less than 0.5 and thus the secant bulk modulus is positive. For the bulk modulus of the saturated samples, an increase is seen with decreasing temperature while the value at 15℃ is seen to be lower in the saturated sample compared to the dry sample. Considering the shear modulus (Fig. 9b), both tangent and secant calculations show the same behaviour moving from the dry to the saturated condition. However, using tangent values under saturated conditions, the shear modulus achieved its peak at -5℃ in contrast to the secant shear modulus that achieved its maximum at -10 ℃ and

showed an increasing trend with reduction in temperature. This indicates that the selected slopes of the curves can have a significant influence on the outcomes for the properties of the material.

Comparison between the results of Wood's (1990) and ISRM method are presented for the UCS test in Fig. 9 and Table 3. In this way, the robustness of Wood's (1990) method in describing the UCS tests can be demonstrated. Triaxial test results, where only Wood's (1990) method is applicable due to confinement can then be compared to UCS outcomes. The assumption made is that during the UCS test the deviatoric stress is equal to axial stress and the confining pressure is set equal to zero.

3.2 Triaxial Results

Results from the triaxial tests for the saturated samples are presented in this section in Figs. 10, 11, 12, 13, 14 and 15. The different calculated moduli using the Wood's (1990) method are presented for 12.5 MPa and 24 MPa confinement in Tables 3 and 4, respectively. Diagonal fractures indicative of shear failure were typical. In contrast to the UCS tests, all the results were in good agreement to each other as the increase in volume during grain crushing was limited because of confinement.
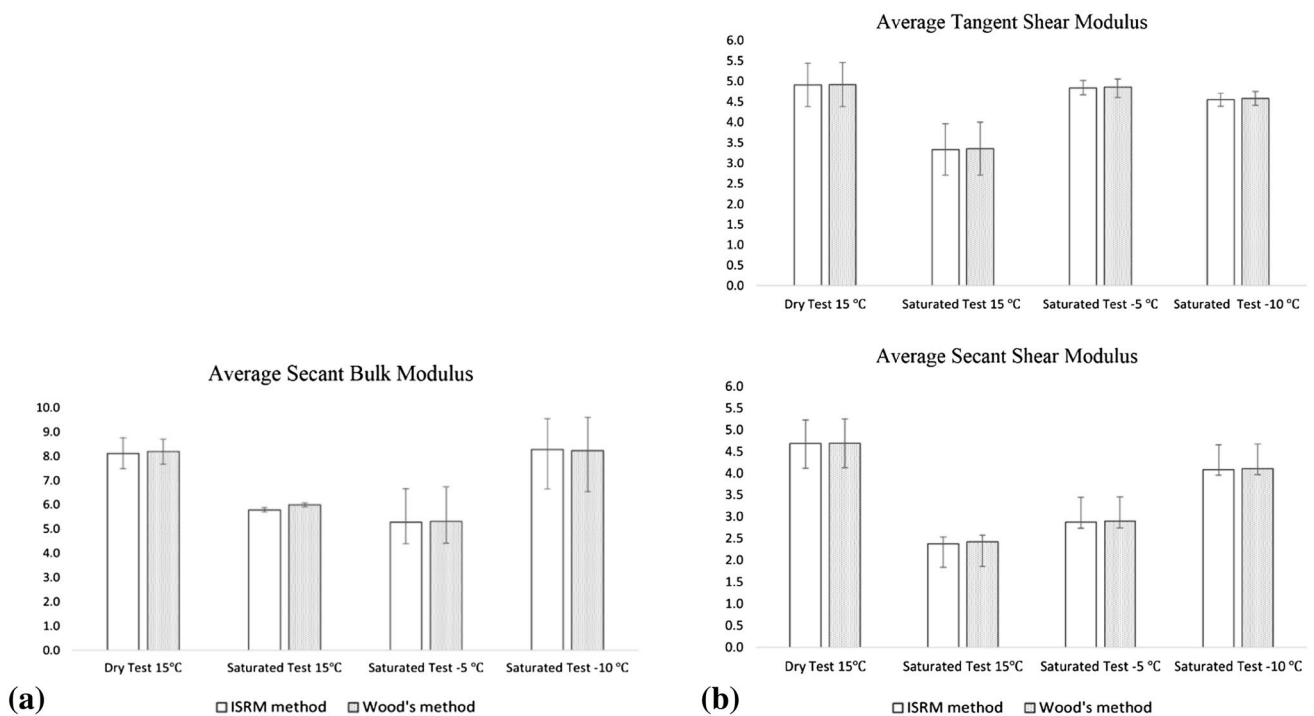

Fig. 9 **a** Average Secant Bulk Modulus K (GPa) for different tested temperatures using both methods (ISRM and Wood's). **b** Average Tangent and Secant Shear Modulus G (GPa) for different tested tem-peratures using both methods (ISRM and Wood's). Whiskers indicate the maximum and minimum calculated value
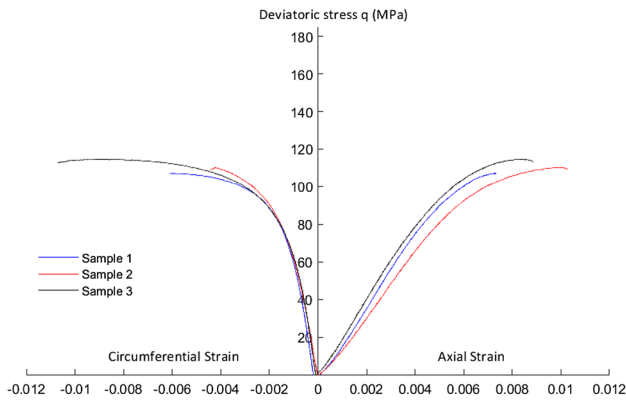
Fig. 10 Diagram of vertical and lateral strain versus deviatoric stress for 12.5 MPa confining pressure representing 500 m depth of the wellbore. Temperature 15 ℃
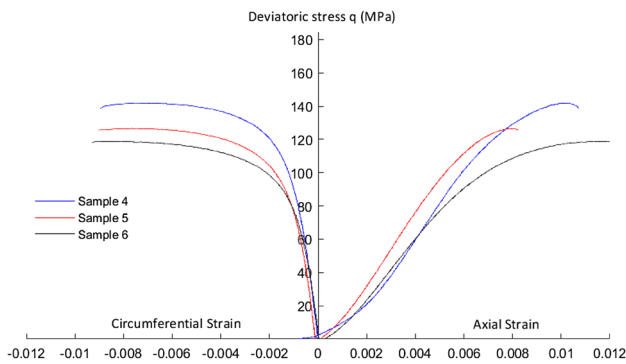

Fig. 12 Diagram of vertical and lateral strain versus deviatoric stress for the 12.5 MPa confining pressure Case with temperature – 10 ℃

Fig. 11 Diagram of vertical and lateral strain versus deviatoric stress for 12.5 MPa confining pressure representing 500 m depth of the wellbore. Temperature – 5 ℃

Fig. 13 Diagram of vertical and lateral strain versus deviatoric stress for 24 MPa confining pressure representing 1000 m depth of the wellbore. Temperature 15 ℃

Fig. 14 Diagram of vertical and lateral strain versus deviatoric stress for 24 MPa confining pressure representing 1000 m depth of the wellbore. Temperature – 5 ℃

The effect of temperature on the mechanical properties of Stainton sandstone is significant. It can be mentioned that in Figs. 10, 11, 12, 13, 14 and 15 moving from 15 ℃ to sub-zero temperatures (– 5 ℃ and – 10 ℃), the strength of the sandstone samples increases for constant confinement, in agreement with Zhang et al. (2019). According to the 12.5 MPa triaxial results, an increase in the peak deviatoric stress with temperature drop from 15 to – 5 ℃ of approximately 20%, is estimated. Analysing the 24-MPa triaxial results, the deviatoric stress increased almost 10% for the same decrease in temperature. For both confining pressures, the maximum deviatoric stress is hardly influenced by further temperature drop from – 5 ℃ to – 10 ℃, as seen in Tables 4 and 5. Shear and bulk modulus, for the three temperatures, follow the same trend for both confining pressures, where the shear modulus increases with temperature decrease, while the bulk modulus decreases. It should be noted that, as ice forms, the strength of the rock increases, however the Poisson's ratio decreases, making the material more
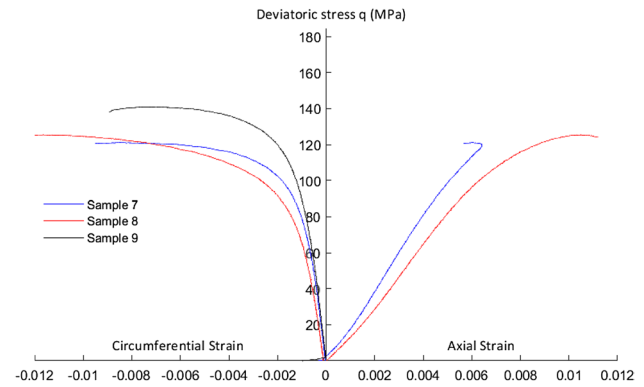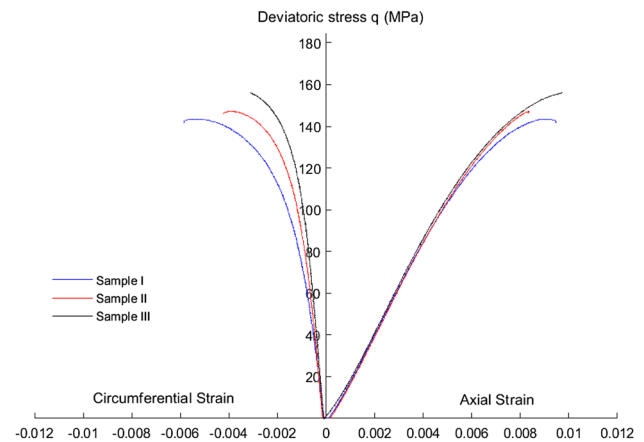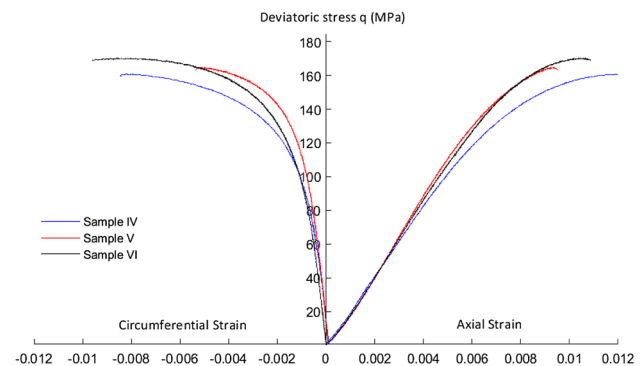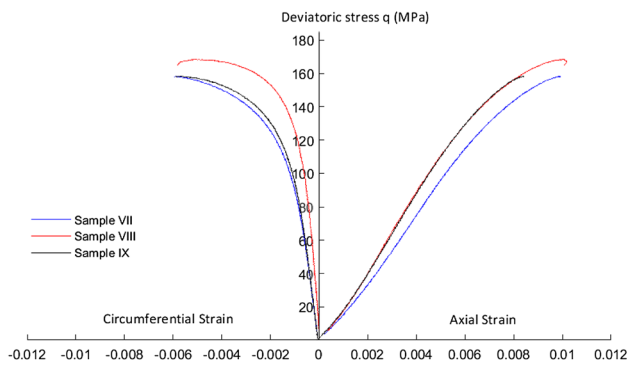
Fig. 15 Diagram of vertical and lateral strain versus deviatoric stress for 24 MPa confining pressure representing 1000 m depth of the wellbore. Temperature – 10 ℃

Table 4 Mechanical calculated properties for Triaxial test 12.5 MPa confining pressure

Sample ID	Max q (MPa)	E (GPa)	v	G (GPa)	K (GPa)
15 ℃ temperature					
Sample 1	107.09	20.67	0.37	7.55	26.35
Sample 2	110.25	17.96	0.36	6.60	21.60
Sample 3	114.51	19.69	0.39	7.10	29.51
–5 ℃ temperature					
Sample 4	141.54	21.81	0.25	8.76	14.34
Sample 5	126.72	22.33	0.27	8.74	16.86
Sample 6	118.83	18.04	0.26	7.04	13.48
– 10 ℃ temperature					
Sample 7	121.18	18.27	0.30	6.99	15.86
Sample 8	125.50	21.73	0.27	8.52	15.49

Table 5 Mechanical calculated properties for Triaxial test 24 MPa confining pressure

Sample ID	Max q (MPa)	E (GPa)	v	G (GPa)	K (GPa)
15 ℃ temperature					
Sample I	143.48	23.09	0.29	8.97	18.25
Sample II	147.34	22.08	0.26	8.79	15.35
Sample III	156.08	23.02	0.26	9.65	12.70
– 5 ℃ temperature					
Sample IV	160.89	21.09	0.26	8.36	15.30
Sample V	164.90	24.57	0.22	10.10	14.84
Sample VI	170.29	23.33	0.25	9.32	15.82
– 10 ℃ temperature					
Sample VII	158.31	21.14	0.23	8.66	14.46
Sample VIII	168.38	23.98	0.19	10.08	13.05
Sample IX	158.37	23.84	0.23	9.69	15.78
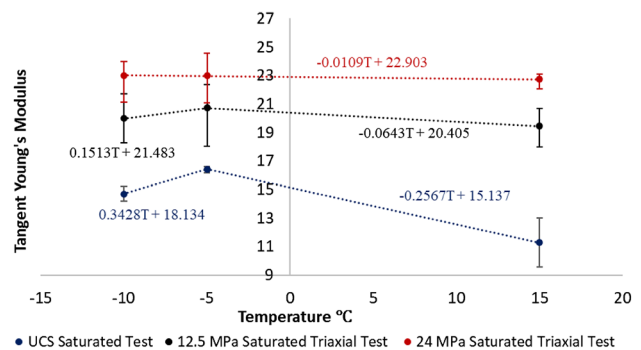
Fig. 16 Average tangent Young's modulus at different confining pressures and temperatures

brittle and potentially induce damage easier. In contrast to the UCS test, where dilation occurs, the rock does not increase in volume and consequently Poisson's ratio remains under the elastic limit of 0.5. The average shear modulus increases with temperature decrease, while the bulk modulus fluctuates for the – 5 ℃ triaxial condition. This is mainly happening as the calculation varies according to the selected slope and due to differences in the deviatoric stress-vertical strain curves. This dissimilarity may occur due to stretching of the rock caused by the application of confining pressure prior to reaching isotropic conditions.

Effects of the confining pressure to the triaxial results are also discussed. Comparison between the 12.5 MPa and 24 MPa tests, is achieved. Increasing the confinement pressure, for certain temperature condition, the strength of sandstone increases significantly up to 40%. Additionally, Young's modulus is higher and the Poisson's ratio lower for higher confining pressure (24 MPa) compared to lower confining pressure (12.5 MPa). Finally, it is worth mentioning that for 12.5 MPa confinement, the reduction in the bulk modulus is much larger than for 24 MPa, indicating that lower confinement has higher compressibility.

3.3 Effects of Temperature and Pressure on Young's Modulus and Poisson's Ratio

Figures 16 and 17 show how the tangent Young's modulus and Poisson's ratio vary with temperature for the different tests. Functions fitted to the data points are also presented in the figures with an assumption of linear variation between the points based on the research of Wang et al. (2019a). For a temperature decrease from 15 to – 5 ℃, the tangent Young's modulus calculated for UCS conditions is 75% higher than the tangent Young's modulus at 12.5 MPa confining conditions, and 96% higher than the tangent Young's modulus at the 24 MPa confining conditions. This trend follows the findings of Wang and Zhang (2021) although it is clear that there is a significant change in behaviour between – 5 and – 10 ℃.

For tangent Poisson's ratio, when moving from 15 to – 5 ℃ a slight change is seen for both the UCS and 24 MPa
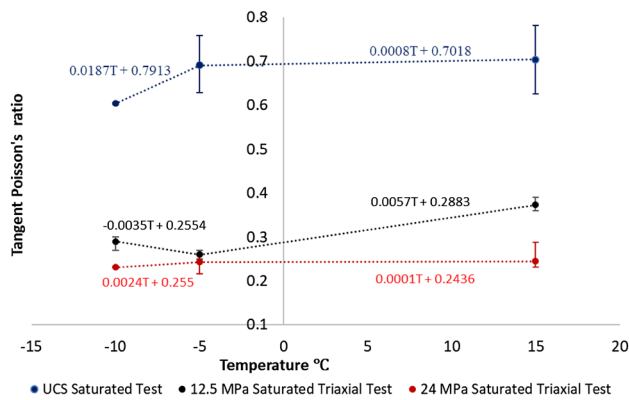
Fig. 17 Average Poisson's at different confining pressures and temperatures

confining test (Fig. 17). In the 12.5 MPa confinement test a decrease of tangent Poisson's ratio is seen. Further temperature reduction indicates a significant reduction, an increase and a slight decrease in tangent Poisson's ratio for the UCS, 12.5 MPa confinement and 24 MPa confinement cases respectively. The UCS test seems to be the most sensitive to temperature effects for both Young's modulus and Poisson's ratio.

4 Critical State Mechanics

For use in future numerical modelling and to facilitate geomechanical modelling that employs critical state mechanics (e.g., Dafalias and Herrmann 1986; Khalili et al. 2005; Ma et al. 2022), the slope of the critical state line is here estimated based on the UCS and triaxial tests above. Studying the temperature influence on the critical state line is important, as it defines the elastic behaviour limit and the yield surface in the $q - p'$ domain and can be used as an input in future numerical simulations (Wood 1990; Shah 1997). The slope of the critical state line M_{cs} is the slope of the failure line where compactive and dilatant strains are equal (Rutter and Glover 2012).

Based on the research of Khalili et al. (2005), Ma (2014), Reppas et al. (2020, 2022), critical state mechanics and bounding surface model seem to work satisfactorily in the reproduction of the experimental results. The bounding surface based on Khalili et al. (2005) is expressed as follows:

$$\frac{q}{M_{cs}p'} - \left(\frac{\ln\left(\frac{p_{co}\prime}{p'}\right)}{\ln R}\right)^{\frac{1}{M}} = 0, \tag{8}$$

where $p\prime$ represents the current effective stress on the yield surface, $p_{co}\prime$ controls the size of the bounding surface (and is the maximum pre-consolidated pressure), M controls the shape of the bounding surface and R is a material constant that is the ratio between $p_{co}\prime$ and the current stress p' at the intersection point of the yield function and critical state line in the $q - p'$ domain.

In Fig. 18 the bounding yield surface, the critical state line, the loading pathways in $q - p'$ domain and the yield points are presented. Based on the research of Schultz et al. (2010), for a porosity of 17% and a grain size of 0.15 mm, the pre-consolidation pressure is estimated to be 240 MPa. The material constant R is estimated to be equal to 2 as the ratio between the pre-consolidated pressure and the current stress at the intersection of the yield function and the critical state line in the $q - p'$ domain (Ma 2014).

5 Microstructural Analysis

In this section, microstructural characterisation of sample in both natural and deformed states is presented. Analysis of the deformation and failure mechanisms allows for insights as to how rock in the near wellbore region may fail during drilling or injection operations.

A significant finding noted above was that, under the uniaxial compression tests conducted in this study the Poisson's ratio exceeded the permitted linear value, i.e., it was > 0.5. A proposed explanation to this is that the samples underwent significant dilation during deformation. To investigate this, the microstructural development of the samples was studied. To understand the origins of the mechanical behaviours observed during the deformation experiments, a microstructural characterisation of the sandstone was first undertaken on an undeformed core as a control. Similar examinations were then performed on samples tested to failure under UCS and 12.5 MPa confining pressure triaxial conditions.

5.1 Microstructural Analysis of Undeformed Sample

Optical microscopy images of the undeformed sample taken on thin sections under plane and crossed polarised light conditions are shown in Fig. 19. Figure 19a shows a representative undeformed sample microstructure under low magnification (× 100) perpendicular to the axis of the core under plane-polarised (PPL) and crossed-polarised (XPL) lights. Figure 19b, c shows the undeformed sample under high magnification (× 400) taken parallel to the axis of the core. It is revealed that a tightly packed microstructure largely comprised of quartz, present as well-sorted subangular to subrounded grains between 100 and 150 microns in size. Occasional lithic fragments (Fig. 19a) and ribbons
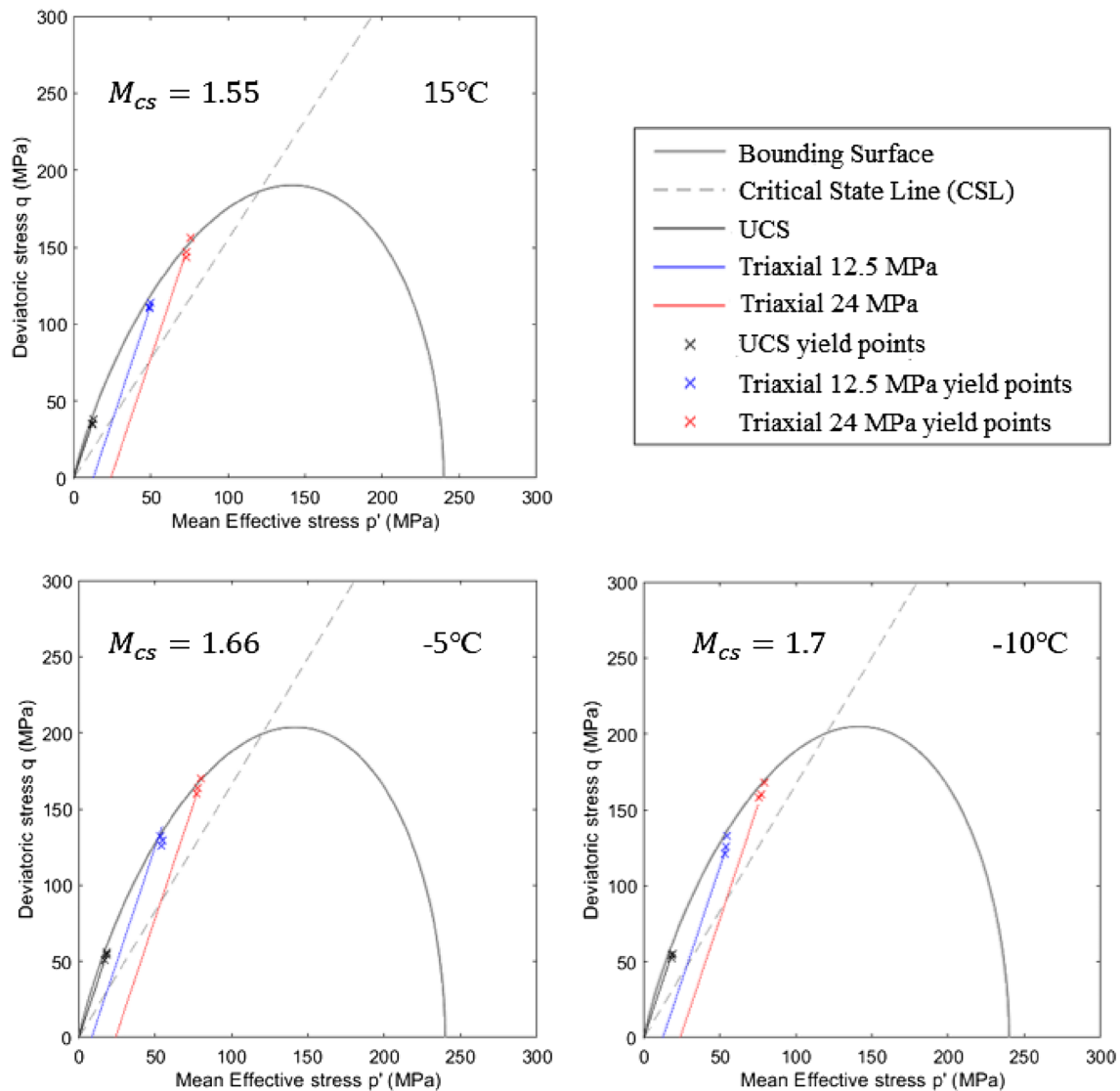
Fig. 18 Bounding surface model and slope of Critical State line (M_{cs}) for three different tests

of muscovite mica are presented throughout the sample (Fig. 19b). Iron oxide coatings are ubiquitous throughout, forming dusty rims to quartz grains, and is locally pore filling (Fig. 19a). Syntaxial quartz cements are also present, generally confined to pore throats, and only developed where ferric coatings are absent. This implies coexistence of clay minerals with the ferric oxides. These are likely illite–smectite, which are well-known to act as inhibitors to authigenic quartz growth (Fisher et al. 1999; Worden and Burley 2003; Busch et al. 2017).

Under purely mechanical compaction, well-sorted sandstones can be expected to reach porosities of 26% (Worden and Burley 2003). The low porosity of 17% recorded for this sandstone suggests additional chemically enhanced compaction of the sample. This is evidenced by quartz grain boundaries that display irregular grain contact geometries

(Fig. 19b). This is indicative of pressure solution at grain contacts during burial. The irregular contacts promote geometric interlocking of grains and increased contact area between grains. There is also local evidence of grain suturing shown by a marked contrast in XPL (Fig. 19b) interference colours in what PPL (Fig. 19c) shows as a single grain. This reflects the differing orientations of the two parent grains that have become fused through chemically enhanced compaction. It is likely that the enhanced intergrain contacts and local contacts because of pressure solution, would contribute to the overall frictional strength characteristics of the material and may act as a major control on material strength in comparison to the comparatively poorly developed syntaxial quartz cements and pore filling quartz. The clay–mineral + ferric oxide coats and pore filling cements would not
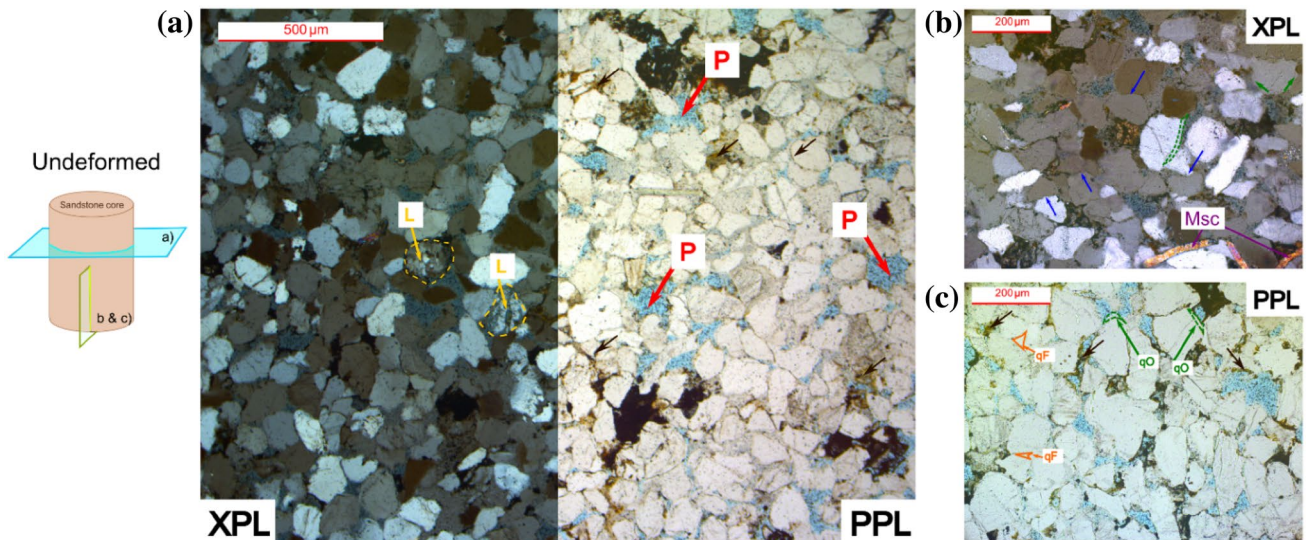
Fig. 19 Optical microscopy images of the studied sandstone taken under plane-polarised (PPL) and crossed-polarised (XPL) light conditions in the undeformed reference state. **a** Low magnification (×100) perpendicular to the axis of the core under PPL and XPL. **b**, **c** Crossed-polarised high magnification (×400) of the undeformed sample taken parallel to the axis of the core. Symbols in the figure are as follows; pore space (P); lithic fragment (L); syntaxial quartz overgrowths (qO, outlined in green); quartz fill (qF, orange outline); muscovite mica (Msc); iron oxide grin coatings (brown arrows); sutured grain-grain contacts (blue arrow). The orientation of panels (**a–c**) relative to the axis of the sample core are show in the schematic to the left of the figure. No experimental stresses were applied to this sample

be expected to contribute significantly to the overall material strength (Fisher et al. 1999).

5.2 Microstructural Analysis of the UCS Tested Sample

Microscopy images of the sample tested under the UCS conditions show some significant differences and evidence of damage. In the far field (Fig. 20c), sample porosity remains close to that of the undeformed sample (Fig. 19a). This contrasts with Fig. 19a, where porosity near the damage zone appears reduced. Grains showed little internal brittle deformation, with intra-granular microcracks absent. Blue arrows (Fig. 20) highlight the alignment of the long axis of grains and dilatant boundaries are identified by the "jigsaw" like parting between adjacent grains. There is some degree of undulous extinction present implying permanent twisting to the crystal lattice during deformation. Operation of such crystal-plastic mechanisms acts to promote work hardening, and arrest of microcrack development (Rutter 1986; Menéndez et al. 1996). This implies that failure during unconfined conditions was primarily accommodated by shearing of quartz cements before sufficient strain was achieved within the grains to initiate internal fracture. Figure 20a, b show evidence of parting along grain-to-grain contacts, (marked dB). Note from Fig. 19a, that the irregular contacts between grains are only rarely fully sutured. Figure 20b shows evidence of particle alignment, with a sub-parallel arrangement of the long axes of elongate quartz grains evident. This is also seen more widely in the rest of the damage zone (Fig. 20a). Combined, these microstructural observations provide evidence of shear enhanced particle-to-particle sliding and realignment. Such processes contribute a mechanism by which an increase in sample volume can occur after shearing of quartz cements.

5.3 Microstructural Analysis of the Triaxial Tested Sample

In the uniaxially deformed sample, there is evidence for inter-grain rotation through alignment of the grain long-axes, which acts to promote sample dilation after initial shearing of cements and explain the inferred value of Poisson's ratio that is beyond the limit assuming linear elasticity. However, in the triaxially deformed sample, there is prevalent intragranular micro-cracking observed (red arrows) (Fig. 21a) that is not present in the undeformed material (Fig. 19a). This is present throughout the sample but increases in intensity towards the damage zone (Fig. 21b). This is due to increased contact stresses preventing inter-grain slip (Menéndez et al. 1996). Lack of inter-grain sliding seeks to prevent volumetric dilation of the sample during loading. Although, grain size reduction could also be interpreted as evidence against dilation through pore collapse, this is generally only possible where such mechanisms accompany macroscopically
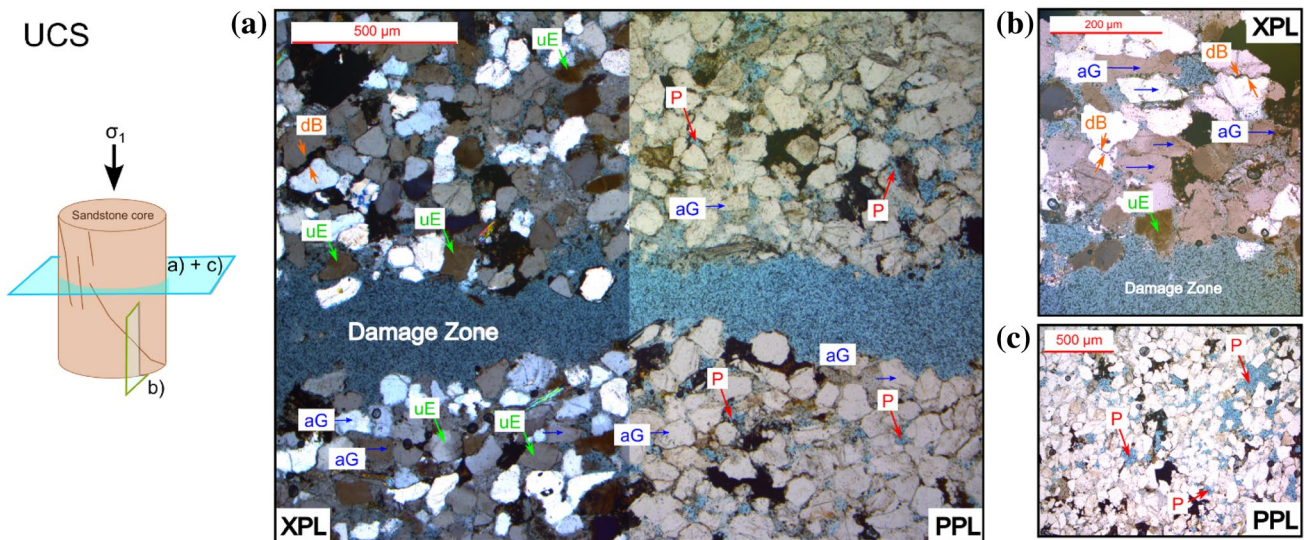
Fig. 20 Optical microscopy images of the sandstone deformed under uniaxial conditions. **a** Plane and crossed polarised light (PPL and XPL) images showing the experimentally formed damage zone at sample failure. **b** Higher magnification view under XPL adjacent to the damage zone. **c** PPL image in a region distant to the experimentally formed damage zone for comparison to panels (**a**, **b**). Symbols in the figure are as follows: pore space (P); undulose extinction (uE); dilatant boundary (dB); alignment of grains (aG). The orientation of panels (**a**–**c**) relative to the axis of the sample core and relative to the applied stress (σ_1) is shown in the schematic to the left of the figure. For UCS conditions, $\sigma_3 = 0$

ductile deformation (Rutter 1986). Instead, the samples deformed under 12.5 MPa confining stress display clear shear localization and macroscopically brittle deformation (Fig. 21). Therefore, the apparent compaction observed in the fine-grained region likely occurs due to late stage collapse of the sample during shear localization from microcracking (Menéndez et al. 1996) rather than as a controlling deformation mechanism in its own right.

Note that the samples deformed under 24 MPa confining pressure also result in a discrete fracture plane, rather than diffuse internal deformation. This is due to the experimental conditions of these tests resulting in an intersection of the yield surface on the shear side rather than the cap side. Therefore, the deformation mechanisms controlling failure in these samples are expected to be similar, although microcracking would be more intense. Finally, more intense micro-cracking indicates decrease in the Poisson's ratio, which also validates the experimental results of Fig. 17.

6 Conclusions

The effect of sub-zero temperatures on the mechanical behaviour of Stainton sandstone has been investigated through a series of uniaxial and triaxial compression tests. ISRM and Wood's (1990) methods showed similar results for the mechanical properties of rock. The results confirmed that the sandstone presents an elastoplastic behaviour with strong dependency on the confining pressure and temperature conditions. Depending on the method of calculation, Poisson's ratio for the UCS test, representative of the conditions at wellbore head, can be larger than 0.5 due to dilation of the material and grain realignment, as demonstrated by microscopic analysis before and after the tests.

For UCS and relatively low confinement (12.5 MPa) conditions, cooling causes an increase in Young's modulus down to − 5 ℃, followed by a reduction with further decrease of temperature. For higher confining pressures (24 MPa), Young's modulus is not affected by changes in temperature. However, a reduction in Poisson's ratio and a decrease in the dilation of the material is seen with decreasing temperature, while the slope of the critical state line increases.

Extrapolating the experimental results to CCS conditions, it can be seen that freezing the sandstone can increase the Young's modulus of the rock, as well as the shear and bulk moduli, especially at the seabed, which is best represented by the UCS test results. Lower temperatures can increase the strength of the rock but also decrease Poisson's ratio, which indicates that the rock may be fractured more easily due to a loss of ductility.

Mathematical functions have been determined from these results for use in modelling. Additional testing would help constrain their variability. Relationships linking the

Fig. 21 Optical microscopy images of a sample deformed under triaxial conditions with a confining stress of $\sigma_3 = 12.5$ MPa. **a** Experimental damage zone under both XPL and PPL conditions. **b** Higher resolution of damage zone under crossed polarized light. Symbols used in figure are as follows: undulose extinction (uE); grain size reduction (GSR). Both images are taken perpendicular to the axis of the sample, and to the direction of the applied maximum stress (σ_1)
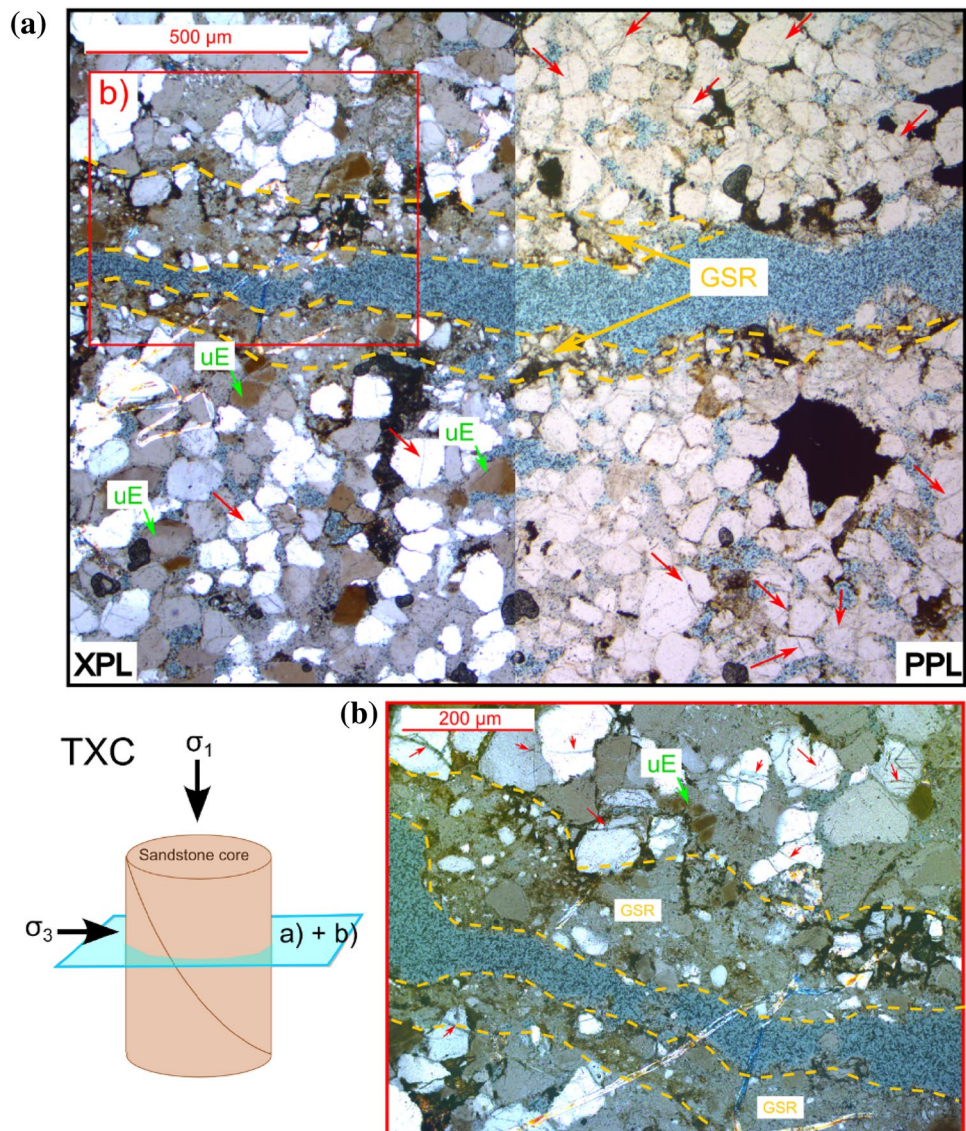
temperature to the mechanical parameters can be implemented in robust Thermo-Hydro-Mechanical models to predict the behaviour of the rock in the vicinity of the wellbore during CO_2 injection.

Author Contributions All authors contributed to the study conception and design. Material preparation and data collection were performed by NR and CD. Analysis of the results was performed by NR. BW and YG contributed to the presentation of the results. SG contributed to the microscopic analysis of the samples. The first draft of the manuscript was written by NR and all authors commented on previous versions of the final manuscript. All authors read and approved the final manuscript.

Data availability Data are availlable upon request.

Declarations

Conflict of Interest All authors certify that they have no affiliations with or involvement in any organization or entity with any financial interest or non-financial interest in the subject matter or materials discussed in this manuscript.

References

Agada S, Jackson S, Kolster C, Dowell NM, Williams G, Vosper H, Williams J, Krevor S (2017) The impact of energy systems demands on pressure limited CO2 storage in the Bunter Sandstone of the UK Southern North Sea. Int J Greenh Gas Control 65:128–136

Armitage P, Faulkner D, Worden R, Aplin A, Butcher A, Iliffe J (2011) Experimental measurement of, and controls on, permeability and permeability anisotropy of caprocks from the CO2 storage project at the Krechba Field, Algeria. J Geophys Res Solid Earth 116:B12208

Aursand P, Hammer M, Lavrov A, Lund H, Munkejord ST, Torsæter M (2017) Well integrity for CO2 injection from ships: simulation of the effect of flow and material parameters on thermal stresses. Int J Greenh Gas Control 62:130–141

Bai Y, Shan R, Ju Y, Wu Y, Sun P, Wang Z (2020) Study on the mechanical properties and damage constitutive model of frozen weakly cemented red sandstone. Cold Reg Sci Technol 171:102980

Barrio M, Aspelund A, Weydahl T, Sandvik TE, Wongraven LR, Krogstad H, Henningsen R, Mølnvik M, Eide SI (2005) Ship-based transport of CO2. In: Rubin ES, Keith DW, Gilboy CF, Wilson M, Morris T, Gale J, Thambimuthu K (eds) Greenhouse gas control technologies 7. Elsevier Science Ltd, Oxford

Bs (2015) Code of practice for ground investigations. British Standards Institution London

Busch B, Hilgers C, Gronen L, Adelmann D (2017) Cementation and structural diagenesis of fluvio-aeolian Rotliegend sandstones, northern England. J Geol Soc 174:855–868

Carrera J, Silva O, Rötting T, Carbonell R, Vilarrasa V, Pérez-Estaún A, Group CSR (2011) Characterization and working programme of Hontomín CO2 injection site (Spain). Monitoring, hydrogeochemical characterization and injection tests

Chadwick R, Zweigel P, Gregersen U, Kirby G, Holloway S, Johannessen P (2004) Geological reservoir characterization of a CO2 storage site: the Utsira Sand, Sleipner, northern North Sea. Energy 29:1371–1381

Cuss R, Rutter E, Holloway R (2003) The application of critical state soil mechanics to the mechanical behaviour of porous sandstones. Int J Rock Mech Min Sci 40:847–862

Dafalias YF, Herrmann LR (1986) Bounding surface plasticity. II: Application to isotropic cohesive soils. J Eng Mech 112:1263–1291

Dong L, Xu H, Fan P, Wu Z (2021) On the experimental determination of Poisson's ratio for intact rocks and its variation as deformation develops. Adv Civ Eng 2021:10. https://doi.org/10.1155/2021/8843056

Eiken O, Ringrose P, Hermanrud C, Nazarian B, Torp TA, Høier L (2011) Lessons learned from 14 years of CCS operations: Sleipner, In Salah and Snøhvit. Energy Procedia 4:5541–5548

Everall TJ, Sanislav IV (2018) The influence of pre-existing deformation and alteration textures on rock strength, failure modes and shear strength parameters. Geosciences 8:124

Fakhri D, Mahmoodzadeh A, Mohammed AH, Khodayari A, Ibrahim HH, Rashidi S, Karim SHT (2023) Forecasting failure load of Sandstone under different Freezing-Thawing cycles using Gaussian process regression method and grey wolf optimization algorithm. Theoret Appl Fract Mech 125:103876

Fisher QJ, Casey M, Clennell MB, Knipe RJ (1999) Mechanical compaction of deeply buried sandstones of the North Sea. Mar Pet Geol 16:605–618

Gerogiannopoulos N, Brown E (1978) The critical state concept applied to rock. Int J Rock Mech Min Sci Geomech Abstr 15(1):1–10

Gluyas JG, Bagudu U (2020) The endurance CO2 storage site, blocks 42/25 and 43/21, UK North Sea. Geol Soc Lond Memoirs 52:163–171

Hangx S, Van Der Linden A, Marcelis F, Bauer A (2013) The effect of CO2 on the mechanical properties of the Captain Sandstone: Geological storage of CO2 at the Goldeneye field (UK). Int J Greenh Gas Control 19:609–619

Hansen O, Gilding D, Nazarian B, Osdal B, Ringrose P, Kristoffersen J-B, Eiken O, Hansen H (2013) Snøhvit: the history of injecting and storing 1 Mt CO2 in the fluvial Tubåen Fm. Energy Procedia 37:3565–3573

Haszeldine RS (2009) Carbon capture and storage: how green can black be? Science 325:1647–1652

Hawkins P (1978) Relationship between diagenesis, porosity reduction, and oil emplacement in late Carboniferous sandstone reservoirs, Bothamsall Oilfield, E Midlands. J Geol Soc 135:7–24

Hawkins AB (1998) Aspects of rock strength. Bull Eng Geol Env 57:17–30

Heinemann N, Wilkinson M, Pickup GE, Haszeldine RS, Cutler NA (2012) CO2 storage in the offshore UK Bunter Sandstone Formation. Int J Greenh Gas Control 6:210–219

Hoek E, Brown ET (1980) Empirical strength criterion for rock masses. J Geotech Eng Div 106:1013–1035

Huang S, Yu S, Ye Y, Ye Z, Cheng A (2022) Pore structure change and physico-mechanical properties deterioration of sandstone suffering freeze-thaw actions. Constr Build Mater 330:127200

Jin M, Pickup G, Mackay E, Todd A, Sohrabi M, Monaghan A, Naylor M (2012) Static and dynamic estimates of CO2-storage capacity in two saline formations in the UK. SPE J 17:1108–1118

Kazemi H (1969) Pressure transient analysis of naturally fractured reservoirs with uniform fracture distribution. Soc Petrol Eng J 9:451–462

Khalili N, Habte M, Valliappan S (2005) A bounding surface plasticity model for cyclic loading of granular soils. Int J Numer Methods Eng 63:1939–1960

Kodama J-I, Mitsui Y, Hara S, Fukuda D, Fujii Y, Sainoki A, Karakus M (2019) Time-dependence of mechanical behavior of Shikotsu welded tuff at sub-zero temperatures. Cold Reg Sci Technol 168:102868

Kong B, Wang E, Li Z, Wang X, Liu X, Li N, Yang Y (2016) Electromagnetic radiation characteristics and mechanical properties of deformed and fractured sandstone after high temperature treatment. Eng Geol 209:82–92

Leeder MR, Hardman M (1990) Carboniferous geology of the Southern North Sea Basin and controls on hydrocarbon prospectivity. Geol Soc Lond Spec Publ 55:87–105

Li X, Xu R, Wei L, Jiang P (2015) Modeling of wellbore dynamics of a CO2 injector during transient well shut-in and start-up operations. Int J Greenh Gas Control 42:602–614

Liping W, Ning L, Jilin Q, Yanzhe T, Shuanhai X (2019) A study on the physical index change and triaxial compression test of intact hard rock subjected to freeze-thaw cycles. Cold Reg Sci Technol 160:39–47

Liu B, Sun Y, Wang B, Han Y, Zhang R, Wang J (2020) Effect of water content on mechanical and electrical characteristics of the water-rich sandstone during freezing. Environ Earth Sci 79:1–14

Ma J (2014) *Coupled flow deformation analysis of fractured porous media subject to elasto-plastic damage. Ph. D Thesis, The University of New South Wales, Australia.*

Ma J, Zhao G-F (2018) Borehole stability analysis in fractured porous media associated with elastoplastic damage response. Int J Geomech 18:04018022

Ma J, Chen J, Chen W, Huang L (2022) A coupled thermal-elastic-plastic-damage model for concrete subjected to dynamic loading. Int J Plast 153:103279

Małkowski P, Ostrowski Ł, Brodny J (2018) Analysis of Young's modulus for Carboniferous sedimentary rocks and its relationship with uniaxial compressive strength using different methods of modulus determination. J Sustain Min 17:145–157

Martin-Roberts E, Scott V, Flude S, Johnson G, Haszeldine RS, Gilfillan S (2021) Carbon capture and storage at the end of a lost decade. One Earth 4:1569–1584

Masoumi H, Saydam S, Hagan PC (2016) Unified size-effect law for intact rock. Int J Geomech 16:04015059

Masoumi H, Roshan H, Hedayat A, Hagan PC (2018) Scale-size dependency of intact rock under point-load and indirect tensile Brazilian testing. Int J Geomech 18:04018006

Masri M, Sibai M, Shao J-F, Mainguy M (2014) Experimental investigation of the effect of temperature on the mechanical behavior of Tournemire shale. Int J Rock Mech Min Sci 70:185–191

Mathias SA, Hardisty PE, Trudell MR, Zimmerman RW (2009) Screening and selection of sites for CO_2 sequestration based on pressure buildup. Int J Greenhouse Gas Control 3:577–585

Menéndez B, Zhu W, Wong T-F (1996) Micromechanics of brittle faulting and cataclastic flow in Berea sandstone. J Struct Geol 18:1–16

Mukherjee H, Brill JP (1999) Multiphase flow in wells. Memorial Fund of AIME, Society of Petroleum Engineers Inc., Richardson

Nevicato D (2022) CCS projects underway at TotalEnergies. In: Responsabilite et environnement, vol 105, pp 43–49

Oldenburg CM (2007) Joule-Thomson cooling due to CO_2 injection into natural gas reservoirs. Energy Convers Manag 48:1808–1815

Page B, Turan G, Zapantis A, Burrows J, Consoli C, Erikson J, Havercroft I, Kearns D, Liu H, Rassool D (2020) The global status of CCS 2020: vital to achieve net zero

Paterson L, Ennis-King J, Sharma S (2010) Observations of thermal and pressure transients in carbon dioxide wells. In: SPE Annual Technical Conference and Exhibition, 2010. OnePetro

Rao Q-H, Wang Z, Xie H-F, Xie Q (2007) Experimental study of mechanical properties of sandstone at high temperature. J Cent South Univ Technol 14:478–483

Rayward-Smith W, Woods AW (2011) Some implications of cold CO_2 injection into deep saline aquifers. Geophys Res Lett, 38:L06407

Reppas N, Gui Y, Wetenhall B, Davie C, Ma J (2020) Elasto-plastic behavior of rock during temperature drop. Int J Geotech Geol Eng 14:177–184

Reppas N, Davie C, Wetenhall B, Gui YL, Ma J (2022) Numerical simulation of Triaxial experimental results on sandstone using critical state mechanics. 56th U.S. Rock Mechanics/Geomechanics Symposium, ARMA-2022-2184

Rickman R, Mullen MJ, Petre JE, Grieser WV, Kundert D (2008) A practical use of shale petrophysics for stimulation design optimization: All shale plays are not clones of the Barnett Shale. In: SPE Annual Technical Conference and eXhibition, 2008. OnePetro

Romana M, Vásárhelyi B (2007) A discussion on the decrease of unconfined compressive strength between saturated and dry rock samples. In: 11th ISRM Congress, 2007. International Society for Rock Mechanics and Rock Engineering

Roy P, Morris JP, Walsh SD, Iyer J, Carroll S (2018) Effect of thermal stress on wellbore integrity during CO_2 injection. Int J Greenh Gas Control 77:14–26

Rutqvist J (2012) The geomechanics of CO_2 storage in deep sedimentary formations. Geotech Geol Eng 30:525–551

Rutter E (1986) On the nomenclature of mode of failure transitions in rocks. Tectonophysics 122:381–387

Rutter E, Glover C (2012) The deformation of porous sandstones; are Byerlee friction and the critical state line equivalent? J Struct Geol 44:129–140

Schultz RA, Okubo CH, Fossen H (2010) Porosity and grain size controls on compaction band formation in Jurassic Navajo Sandstone. Geophys Res Lett 37:L22306

Segall P, Fitzgerald SD (1998) A note on induced stress changes in hydrocarbon and geothermal reservoirs. Tectonophysics 289:117–128

Shah KR (1997) An elasto-plastic constitutive model for brittle-ductile transition in porous rocks. Int J Rock Mech Min Sci 34:283.e1-283.e13

Shen B, Shi J, Barton N (2018) An approximate nonlinear modified Mohr-Coulomb shear strength criterion with critical state for intact rocks. J Rock Mech Geotech Eng 10:645–652

Shu S, Yao Z, Xu Y, Wang C, Hu K (2023) Mechanical properties and constitutive relationship of cretaceous frozen sandstone under low temperature. Appl Sci 13:4504

Silva O (2015) Non-isothermal flow of CO_2 in injection wells: evaluation of different injection modes

Silva O, Carrera J, Vilarrasa V (2011) An efficient injection concept for CO_2 geological storage. Trondheim CCS Conference, CO_2 Capture, Transport and Storage. 14–16 June 2011, Trondheim, Norway

Singh M, Singh B, Shankar D (2005) Critical state mechanics in nonlinear failure criterion for rocks. J Rock Mech Tunnel Technol 11:13–24

Sun Q, Geng J, Zhao F (2020) Experiment study of physical and mechanical properties of sandstone after variable thermal cycles. Bull Eng Geol Env 79:3771–3784

Sündermann J, Pohlmann T (2011) A brief analysis of North Sea physics. Oceanologia 53:663–689

Sutherland F, Duffy L, Ashby D, Legrand P, Jones G, Jude E (2020) Net zero teesside: subsurface evaluation of endurance. In: 1st Geoscience & Engineering in Energy Transition Conference, 2020. EAGE Publications BV, pp 1–5

Ulusay R (2014) The ISRM suggested methods for rock characterization, testing and monitoring: 2007–2014. Springer

Vilarrasa V, Silva O, Carrera J, Olivella S (2013) Liquid CO_2 injection for geological storage in deep saline aquifers. Int J Greenh Gas Control 14:84–96

Wang H-Y, Zhang Q (2021) Mechanical behavior of frozen porous sandstone under uniaxial compression. Geofluids 2021:1872065

Wang C, Li S, Zhang T, You Z (2019a) Experimental study on mechanical characteristics and fracture patterns of unfrozen/freezing saturated coal and sandstone. Materials (basel, Switzerland) 12:992

Wang H, Wang J, Wang X, Dou F, Hu B (2019b) Coupled hydro-thermal-mechanical analysis for cold CO_2 injection into a deep saline aquifer. Therm Sci 23:917–925

Wood DM (1990) Soil behaviour and critical state soil mechanics. Cambridge University Press, Cambridge

Worden RH, Burley S (2003) Sandstone diagenesis: the evolution of sand to stone. Sandstone Diagenesis Recent and Ancient 4:3–44

Wu J, Wang H, Zong Q, Xu Y (2020) Experimental investigation of dynamic compression mechanical properties of frozen fine sandstone. Adv Civ Eng 2020:1–10

Wu G, Wang Y, Swift G, Chen J (2013) Laboratory investigation of the effects of temperature on the mechanical properties of sandstone. Geotech Geol Eng 31:809–816

Yahaghi J, Liu H, Chan A, Fukuda D (2021) Experimental and numerical studies on failure behaviours of sandstones subject to freeze-thaw cycles. Transport Geotech 31:100655

Yang S-Q, Xu P, Li Y-B, Huang Y-H (2017) Experimental investigation on triaxial mechanical and permeability behavior of sandstone

after exposure to different high temperature treatments. Geothermics 69:93–109

Yang S-Q, Huang Y-H, Tian W-L (2021) Influence of water saturation and real-time testing temperature on mechanical behavior of sandstone under conventional triaxial compression. Rock Mech Rock Eng 54:4355–4367

Yoshinaka R, Osada M, Park H, Sasaki T, Sasaki K (2008) Practical determination of mechanical design parameters of intact rock considering scale effect. Eng Geol 96:173–186

Yu J, Zhang Q, Jia C, Lei M, Zhao C, Pang R, Li Z, Zeng T (2023) Experimental and DEM simulations of the mechanical properties of rock under freeze–thaw cycles. Cold Regions Sci Technol 211:103866

Zhang D, Ranjith P, Perera M (2016) The brittleness indices used in rock mechanics and their application in shale hydraulic fracturing: a review. J Pet Sci Eng 143:158–170

Zhang G, Liu E, Chen S, Zhang D, Liu X, Yin X, Song B (2019) Effects of uniaxial and triaxial compression tests on the frozen sandstone combining with CT scanning. Int J Phys Model Geotech 19:261–274

Zhang D, Lu G, Wu J, Nie W, Ranjith P (2023) Effects of ultralow temperature and water saturation on the mechanical properties of sandstone. Rock Mech Rock Eng 56:3377–3397

Zhu T, Jing H, Su H, Yin Q, Du M, Han G (2016) Physical and mechanical properties of sandstone containing a single fissure after exposure to high temperatures. Int J Min Sci Technol 26:319–325

Ziabakhsh-Ganji Z, Kooi H (2014) Sensitivity of Joule-Thomson cooling to impure CO2 injection in depleted gas reservoirs. Appl Energy 113:434–451

Zoback MD, Zoback ML (2002) Stress in the Earth's lithosphere. Encycl Phys Sci Technol 16:143–154